


















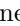




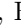






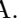
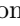

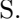


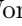

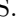


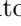




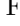



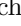
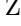
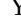
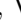




R. Tiwary , D. Tonelli , E. Torassa , K. Trabelsi , I. Tsaklidis , M. Uchida , I. Ueda , Y. Uematsu ,  
T. Uglov , K. Unger , Y. Unno , K. Uno , S. Uno , P. Urquijo , Y. Ushiroda , S. E. Vahsen ,  
R. van Tonder , K. E. Varvell , M. Veronesi , A. Vinokurova , V. S. Vismaya , L. Vitale , V. Vobbiliseti ,  
R. Volpe , B. Wach , M. Wakai , S. Wallner , E. Wang , M.-Z. Wang , X. L. Wang , Z. Wang ,  
A. Warburton , M. Watanabe , S. Watanuki , C. Wessel , E. Won , Y. Xie , X. P. Xu , B. D. Yabsley ,  
S. Yamada , S. B. Yang , J. Yelton , J. H. Yin , K. Yoshihara , C. Z. Yuan , Y. Yusa , L. Zani ,  
F. Zeng , B. Zhang , Y. Zhang , V. Zhilich , Q. D. Zhou , X. Y. Zhou , V. I. Zhukova , and R. Žlebčík 

(The Belle II Collaboration)

We report measurements of time-dependent  $CP$  asymmetries in  $B^0 \rightarrow K_s^0 \pi^0 \gamma$  decays based on a data sample of  $(388 \pm 6) \times 10^6$   $B\bar{B}$  events collected at the  $\Upsilon(4S)$  resonance with the Belle II detector. The Belle II experiment operates at the SuperKEKB asymmetric-energy  $e^+e^-$  collider. We measure decay-time distributions to determine  $CP$ -violating parameters  $S$  and  $C$ . We determine these parameters for two ranges of  $K_s^0 \pi^0$  invariant mass:  $m(K_s^0 \pi^0) \in (0.8, 1.0)$  GeV/ $c^2$ , which is dominated by  $B^0 \rightarrow K^{*0}(\rightarrow K_s^0 \pi^0) \gamma$  decays, and a complementary region  $m(K_s^0 \pi^0) \in (0.6, 0.8) \cup (1.0, 1.8)$  GeV/ $c^2$ . Our results have improved precision as compared to previous measurements and are consistent with theory predictions.

The radiative process  $b \rightarrow s \gamma$  proceeds mainly via a loop amplitude and thus is sensitive to physics beyond the Standard Model (SM) [1–3]. In particular, the polarization of the final-state photon adds unique sensitivity to physics beyond the SM (BSM) [4–11]. In the SM, because a virtual  $W$  boson interacts only with left-handed fermions, the  $s$  quark from  $b \rightarrow s \gamma$  (a  $\bar{B}^0$  decay) is left-handed and thus the outgoing photon must have negative helicity to conserve angular momentum along the decay axis. Similarly, the outgoing photon from a  $B^0$  decay must have positive helicity. The “wrong” photon polarization is possible only if the  $s$  quark flips its chirality, which suppresses this process by a factor of  $m_s/m_b$ . Consequently, mixing-induced  $CP$  violation is expected to be very small in decays governed by the  $b \rightarrow s \gamma$  transition, as the different photon polarizations distinguish between otherwise identical final states originating from  $B^0$  or  $\bar{B}^0$  and thus preclude interference [4, 5]. However, if right-handed currents from BSM physics contribute, a  $B^0$  ( $\bar{B}^0$ ) could more easily emit negative (positive) helicity photons, leading to sizable interference and  $\mathcal{O}(0.1)$  mixing-induced  $CP$  violation [6–11]. For resonant  $B^0 \rightarrow K^*(892)^0(\rightarrow K_s^0 \pi^0) \gamma$  [12], two SM calculations give values  $(-3.5 \pm 1.7) \times 10^{-2}$  [13] and  $(-2.3 \pm 1.6) \times 10^{-2}$  [14] for the  $CP$  asymmetry. Nonresonant  $B^0 \rightarrow K_s^0 \pi^0 \gamma$  decays could include a long-distance contribution from  $b \rightarrow (c\bar{c})s$  rescattering and should be measured separately [15, 16]. In contrast to mixing-induced  $CP$  violation, direct  $CP$  violation in these decays has not been reliably estimated.

Previously, the Belle and *BABAR* experiments measured the mixing-induced  $CP$  asymmetry in  $B^0 \rightarrow K_s^0 \pi^0 \gamma$  decays with a precision of about 30% [17, 18]. These results are consistent with SM predictions, but BSM contributions cannot be excluded. In this Letter, we report new measurements of time-dependent  $CP$  asymmetries in  $B^0 \rightarrow K^*(892)^0 \gamma$  and nonresonant  $B^0 \rightarrow K_s^0 \pi^0 \gamma$  decays using  $362 \text{ fb}^{-1}$  of data [19], corresponding to  $(388 \pm 6) \times 10^6$   $B\bar{B}$  events, recorded by the Belle II

experiment from 2019 to 2022 [20].

Belle II [20] records data at the SuperKEKB collider [21], which collides 7.0 GeV electrons with 4.0 GeV positrons. The detector components most relevant for this measurement are a two-layer silicon-pixel detector (PXD) surrounded by a four-layer double-sided silicon-strip detector (SVD) [22] and a 56-layer central drift chamber (CDC). These detectors reconstruct tracks of charged particles and measure displaced vertices. Only one sixth of the second PXD layer was installed for the data analyzed here. The symmetry axis of these cylindrical detectors, defined as the  $z$  axis, is almost collinear with the direction of the electron beam. The detector coverage is divided into three regions depending on the polar angle  $\theta$ : the barrel region for  $32.2^\circ < \theta < 128.7^\circ$ , and the forward and backward endcaps for  $12.4^\circ < \theta < 31.4^\circ$  and  $130.7^\circ < \theta < 155.1^\circ$ , respectively. Surrounding the CDC is a time-of-propagation counter [23] in the barrel region and an aerogel-based ring-imaging Cherenkov counter in the forward endcap. These detectors provide charged-particle identification (PID). Surrounding the PID detectors is an electromagnetic calorimeter (ECL) based on CsI(Tl) crystals that provides energy and timing measurements for photons and electrons. The sub-detectors described above are enclosed within a superconducting solenoid that provides a 1.5 T magnetic field oriented in the  $z$  direction.

At SuperKEKB, pairs of neutral  $B$  mesons are coherently produced via  $e^+e^- \rightarrow \Upsilon(4S) \rightarrow B^0 \bar{B}^0$ . We reconstruct one  $B$  meson, denoted  $B_{\text{sig}}$ , decaying into  $K_s^0 \pi^0 \gamma$  followed by  $K_s^0 \rightarrow \pi^+ \pi^-$  and  $\pi^0 \rightarrow \gamma \gamma$ . The flavor of  $B_{\text{sig}}$  is opposite to that of the accompanying  $B$  meson, denoted  $B_{\text{tag}}$ , and is determined by a flavor tagging algorithm [24] that outputs  $q = 1$  for  $B_{\text{tag}}^0$  and  $q = -1$  for  $\bar{B}_{\text{tag}}^0$ . The time-dependent (TD) and time-integrated

(TI) decay rates depend on  $q$  and are [25–28]

$$\mathcal{P}_{\text{TD}}(\Delta t, q) = \frac{e^{-|\Delta t|/\tau_{B^0}}}{4\tau_{B^0}} \{1 + q \cdot [S \sin(\Delta m_d \Delta t) - C \cos(\Delta m_d \Delta t)]\}, \quad (1)$$

$$\mathcal{P}_{\text{TI}}(q) = \frac{1}{2} \left[ 1 - q \cdot \frac{C}{1 + \Delta m_d^2 \tau_{B^0}^2} \right], \quad (2)$$

where  $\Delta t \equiv t_{\text{sig}} - t_{\text{tag}}$  is the difference between the proper decay times of  $B_{\text{sig}}$  and  $B_{\text{tag}}$ ,  $S$  and  $C$  are the mixing-induced and direct  $CP$ -violation parameters [29],  $\tau_{B^0}$  is the  $B^0$  lifetime, and  $\Delta m_d$  is the mass difference between the two neutral  $B$ -meson mass eigenstates.

We use Monte Carlo (MC) simulation to optimize event selection criteria, calculate reconstruction efficiencies, and study sources of background. We generate signal MC samples of  $B^0 \rightarrow K^*(892)^0 \gamma$ ,  $B^0 \rightarrow K_2^{*0}(1430) \gamma$ , and  $B^0 \rightarrow K^*(1680) \gamma$ , with the kaonic resonances decaying to  $K_s^0 \pi^0$ , and nonresonant  $B^0 \rightarrow K_s^0 \pi^0 \gamma$  [30]. To model backgrounds, we generate samples of  $e^+ e^- \rightarrow B^0 \bar{B}^0$ ,  $B^+ B^-$ ,  $q \bar{q}$  ( $q = u, d, s, c$ ), and  $\tau^+ \tau^-$ . We use EVTGEN [31] for hadronic decays, KKMC [32] followed by fragmentation by PYTHIA [33] for  $q \bar{q}$ , and TAUOLA [34] for  $\tau$  decays. The detector response is simulated with GEANT4 [35]. We analyze data and MC events using the Belle II software framework [36]. We use Differential Evolution [37] to optimize selection criteria for mass windows, momentum, and boosted decision trees (BDTs), maximizing a figure-of-merit (FoM)  $N_s / \sqrt{N_s + N_b}$ , where  $N_s$  and  $N_b$  are signal and background yields in MC simulation.

To reconstruct the prompt photon, we select a cluster of ECL hits with no associated track. We require that the photon's energy in the center-of-mass (c.m.) frame,  $E_\gamma^*$ , be the highest in the event, and that  $E_\gamma^* > 1.6$  GeV. The dominant background is from photons arising from  $\pi^0$  and  $\eta$  decays; these are rejected with a BDT-based algorithm [38]. We apply a selection on the BDT output that, according to MC simulation, rejects 83% (45%) of photons from  $\pi^0$  ( $\eta$ ) decays while retaining 92% (99%) of prompt signal photons.

We reconstruct  $K_s^0 \rightarrow \pi^+ \pi^-$  candidates using two oppositely charged tracks assumed to be pions. The  $K_s^0$  candidates are selected with an invariant mass in the range  $|m(\pi^+ \pi^-) - m_{K_s^0}| < 34$  MeV/ $c^2$ , where  $m_{K_s^0}$  is the known  $K_s^0$  mass [39]. This range corresponds to  $\pm 2.6\sigma$  in resolution. To further reduce background, we employ another BDT to form two classifiers:  $K_s^0$ -likeness and  $\Lambda$ -likeness, which are based on kinematic and PID information. We apply selection criteria on these classifiers that retain 97% of signal  $K_s^0$  decays, according to MC simulation, while rejecting 67% of candidates due to  $\Lambda$ 's and 98% of other background candidates.

We reconstruct  $\pi^0 \rightarrow \gamma \gamma$  candidates using pairs of ECL clusters with no associated tracks. We require a cluster energy greater than 22.5 MeV in the forward endcap and

greater than 20.0 MeV in other regions. Photon pairs having an invariant mass  $m(\gamma \gamma) \in (104, 164)$  MeV/ $c^2$ , corresponding to  $2\sigma$  in resolution, are selected as  $\pi^0$  candidates. We also require that the  $\pi^0$  momentum exceeds 430 MeV/ $c$ ; this retains 92% of signal  $\pi^0$ 's, according to MC simulation, while rejecting 74% of background  $\pi^0$ 's.

We reconstruct  $B_{\text{sig}}$  candidates by combining  $\gamma$ ,  $K_s^0$ , and  $\pi^0$  candidates. We select  $B_{\text{sig}}$  candidates using the beam-energy-constrained mass  $M_{\text{bc}} \equiv \sqrt{E_{\text{beam}}^{*2}/c^4 - \mathbf{p}_B^{*2}/c^2}$ , and energy difference  $\Delta E \equiv E_B^* - E_{\text{beam}}^*$ , where  $E_{\text{beam}}^*$  is the beam energy and  $E_B^*$  and  $\mathbf{p}_B^*$  are the reconstructed energy and momentum of the  $B_{\text{sig}}$  candidate. All quantities are evaluated in the c.m. frame. We retain  $B_{\text{sig}}$  candidates satisfying  $5.20$  GeV/ $c^2 < M_{\text{bc}} < 5.29$  GeV/ $c^2$  and  $-0.5$  GeV  $< \Delta E < 0.5$  GeV. Almost half (45%) of events have multiple  $B_{\text{sig}}$  candidates, with 96% of these due to multiple  $\pi^0$  candidates. To identify the correct  $B_{\text{sig}}$  candidate, we use a BDT-based classifier based on the properties of the  $\pi^0$  candidate, as described in the Supplemental Material [40]. We retain the  $B_{\text{sig}}$  candidate with the highest  $\pi^0$  BDT classifier value. If multiple candidates share the same  $\pi^0$ , we choose the candidate with the highest value of  $K_s^0$ -likeness. These criteria select the correct  $B_{\text{sig}}$  candidate in 85% of simulated events with multiple candidates. The invariant mass of the  $K_s^0 \pi^0$  system,  $m(K_s^0 \pi^0)$ , is required to be in the range 0.6–1.8 GeV/ $c^2$ . We define mass region 1 (MR1) as  $m(K_s^0 \pi^0) \in (0.8, 1.0)$  GeV/ $c^2$ , which is dominated by the  $K^*(892)^0$  meson, and mass region 2 (MR2) as  $m(K_s^0 \pi^0) \in (0.6, 0.8) \cup (1.0, 1.8)$  GeV/ $c^2$ .

We measure the decay vertex positions of  $B_{\text{sig}}$  and  $B_{\text{tag}}$  in kinematic fits. The  $B_{\text{sig}}$  vertex is determined by a fit to the entire decay chain [41]. This fit includes the constraint that the  $B_{\text{sig}}$  trajectory be consistent with originating from the  $e^+ e^-$  interaction point (IP), within uncertainties. The IP is measured regularly by averaging over samples of  $e^+ e^- \rightarrow \mu^+ \mu^-$  events. For the  $B_{\text{tag}}$  vertex, the tracks used must have a distance of closest approach to the IP within 0.5 cm in the  $r$ - $\phi$  plane and within 2.0 cm along the  $z$  axis. We also require that each track have at least one hit in each of the PXD, SVD, and CDC subdetectors, and a momentum greater than 50 MeV/ $c$ . With these tracks we fit for the  $B_{\text{tag}}$  vertex [42]. To calculate uncertainties on the  $B_{\text{sig}}$  and  $B_{\text{tag}}$  vertices more accurately, we apply corrections to the helix parameter uncertainties of the tracks used in the fits.

We classify events according to the quality of the vertex measurements. Events are classified as ‘‘TD’’ (time-dependent) if they satisfy the following. For the  $B_{\text{sig}}$  vertex, both pions from the  $K_s^0$  must have at least one SVD hit; the  $\chi^2$  of the vertex fit must be less than 30 (100) for tracks (overall); and the uncertainty on  $\ell_{\text{sig}}$ ,  $\sigma_{\ell_{\text{sig}}}$ , must be less than 500  $\mu\text{m}$ . For the  $B_{\text{tag}}$  vertex, the reduced  $\chi^2$  of the vertex fit must be less than 100, and  $\sigma_{\ell_{\text{tag}}}$  must be less than 500  $\mu\text{m}$ . Events that do not satisfy these

criteria are classified as ‘‘TI’’ (time-integrated). For TD events, we calculate the decay time  $\Delta t$  as  $(\ell_{\text{sig}} - \ell_{\text{tag}}) / \beta\gamma c$ , where  $\ell_{\text{sig}}$  ( $\ell_{\text{tag}}$ ) is the  $B_{\text{sig}}$  ( $B_{\text{tag}}$ ) decay vertex position projected along the  $\Upsilon(4S)$  boost direction, and  $\beta\gamma$  is the Lorentz boost factor of the  $\Upsilon(4S)$  in the lab frame.

The flavor  $q$  of  $B_{\text{tag}}$  is determined using a combination of BDT algorithms [24]. The combination outputs the product  $q \cdot r$ , where  $r$  is a quality factor that ranges from zero for no flavor information to 1.0 for unambiguous flavor assignment. As the tagging efficiency and signal purity depend on  $r$ , we divide the data into seven  $r$  bins, each containing a similar number of events. For each  $r$  bin, the wrong-tag fraction  $w$  and the difference  $\Delta w$  between  $B^0$  and  $\bar{B}^0$  tags are determined using a sample of flavor-specific  $B$  decays [43]. The effective tagging efficiency,  $\varepsilon_{\text{eff}} = \sum_i \varepsilon_{\text{tag}}^i (1 - 2w_i)^2$ , is  $(31.69 \pm 0.35)\%$ , where  $\varepsilon_{\text{tag}}^i$  is the probability for a  $B^0 \rightarrow K_s^0 \pi^0 \gamma$  decay to be flavor-tagged with  $r$  in the  $i$ th bin.

We train two BDT classifiers to discriminate signal from  $q\bar{q}$  background, separately for MR1 and MR2 candidates. The classifiers use event topology variables as described in the Supplemental Material [40], and the classifier thresholds are optimized separately for each  $r$  bin. According to MC simulation, these thresholds retain 77% (74%) of signal decays while rejecting 95% (89%) of  $q\bar{q}$  background for MR1 (MR2).

As a control mode, we reconstruct the decay  $B^+ \rightarrow K_s^0 \pi^+ \gamma$  in a similar manner. This decay does not exhibit mixing-induced  $CP$  violation and replicates the vertex resolution of signal decays when the  $\pi^+$  track is ignored.

We determine signal and background yields from an unbinned maximum-likelihood fit to the two-dimensional  $M_{\text{bc}} - \Delta E$  distribution. We fit events in the ranges  $5.23 \text{ GeV}/c^2 < M_{\text{bc}} < 5.29 \text{ GeV}/c^2$  and  $-0.4 \text{ GeV} < \Delta E < 0.3 \text{ GeV}$ , combining the TD and TI samples. We model the  $M_{\text{bc}} - \Delta E$  probability density functions (PDFs) for signal and  $B\bar{B}$  background using MC samples. Kernel density estimation (KDE) [44] is used to account for  $M_{\text{bc}} - \Delta E$  correlations. The  $q\bar{q}$  background is modeled with the product of an ARGUS function [45] for  $M_{\text{bc}}$  and a second-order polynomial for  $\Delta E$ . The signal and  $B\bar{B}$  yields, and the  $q\bar{q}$  shape parameters, are floated in the fit, while the total yield is fixed. To calculate signal yields, we define a signal-enhanced region  $5.27 \text{ GeV}/c^2 < M_{\text{bc}} < 5.29 \text{ GeV}/c^2$  and  $-0.2 \text{ GeV} < \Delta E < 0.1 \text{ GeV}$ . For  $B^0 \rightarrow K^*(892)^0 \gamma$  events, the efficiency in this region is  $(22.8 \pm 0.1)\%$  for MR1. The fitted  $M_{\text{bc}}$  and  $\Delta E$  distributions and projections of the fit result are shown in Fig. 1. The resulting signal and  $B\bar{B}$  yields are listed in Table I. We find a total of 548 events in MR1 and 669 events in MR2.

The  $\Delta t$  PDF consists of signal and background components weighted by their fractions as determined from the  $M_{\text{bc}} - \Delta E$  fit. For the TD category, the PDF is described

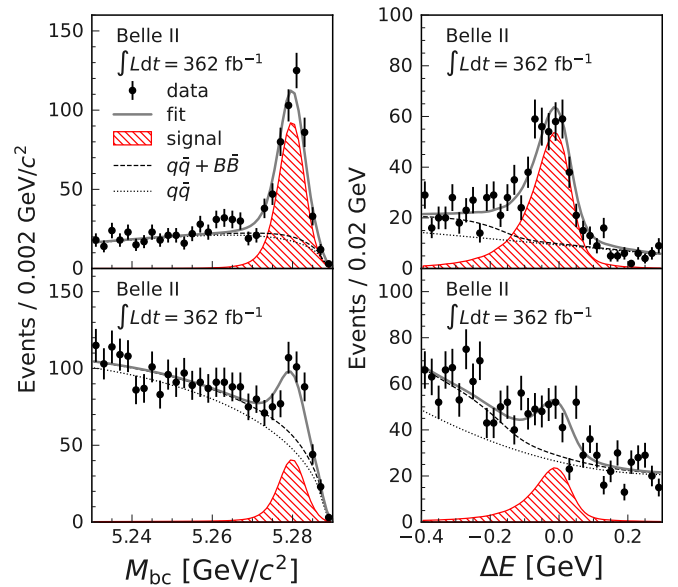


FIG. 1: Distributions of  $M_{\text{bc}}$  (left) and  $\Delta E$  (right) for MR1 (top) and MR2 (bottom), with fit results overlaid. The  $M_{\text{bc}}$  ( $\Delta E$ ) distribution corresponds to the  $\Delta E$  ( $M_{\text{bc}}$ ) signal-enhanced region.

TABLE I: Signal and control sample yields in the signal-enhanced region. Also listed is the ratio of signal to background ( $N_s/N_b$ ), where  $N_b$  includes all backgrounds.

Sample	Signal yield	$B\bar{B}$ bkg yield	$N_s/N_b$
$B^0 \rightarrow K_s^0 \pi^0 \gamma$ in MR1	$385 \pm 24$	$20 \pm 8$	2.36
$B^0 \rightarrow K_s^0 \pi^0 \gamma$ in MR2	$171 \pm 23$	$69 \pm 19$	0.34
$B^+ \rightarrow K_s^0 \pi^+ \gamma$	$843 \pm 34$	$55 \pm 10$	2.68

as

$$\begin{aligned}
 P_{\text{TD}}(\Delta t, q) = & \int_{-\infty}^{\infty} \left[ f_{\text{sig}} \mathcal{P}_{\text{sig}}(\Delta t', q) R_{\text{sig}}(\Delta t - \Delta t') \right. \\
 & \left. + (1 - f_{\text{sig}}) f_{B\bar{B}} \mathcal{P}_{B\bar{B}}(\Delta t', q) R_{B\bar{B}}(\Delta t - \Delta t') \right] d\Delta t' \\
 & + (1 - f_{\text{sig}})(1 - f_{B\bar{B}}) \mathcal{P}_{q\bar{q}}(\Delta t), \quad (3)
 \end{aligned}$$

$$\begin{aligned}
 \mathcal{P}_{\text{sig}}(\Delta t', q) = & \frac{1}{4\tau_{B^0}} e^{-\frac{|\Delta t'|}{\tau_{B^0}}} \left\{ 1 - q\Delta w + q(1 - 2w) \right. \\
 & \left. \times [S \sin(\Delta m_d \Delta t') - C \cos(\Delta m_d \Delta t')] \right\}, \quad (4)
 \end{aligned}$$

$$\mathcal{P}_{B\bar{B}}(\Delta t', q) = \frac{1}{4\tau_{B\bar{B}}} e^{-\frac{|\Delta t'|}{\tau_{B\bar{B}}}} (1 - q\Delta w), \quad (5)$$

where  $f_{\text{sig}}$  is the event-by-event signal probability,  $f_{B\bar{B}}$  is the  $B\bar{B}$  background probability relative to that of all background components,  $\mathcal{P}_{\text{sig}}(\Delta t', q)$  and  $\mathcal{P}_{B\bar{B}}(\Delta t', q)$  are the signal and  $B\bar{B}$  background PDFs taking into account the effect of  $w$  and  $\Delta w$ ,  $\mathcal{P}_{q\bar{q}}(\Delta t)$  is the  $q\bar{q}$  PDF, and  $R_{\text{sig}}$  and  $R_{B\bar{B}}$  are the proper-time resolution functions

for signal and  $B\bar{B}$  background as described in the Supplemental Material [40]. We fix  $\tau_{B^0}$  and  $\Delta m_d$  to world average values [39] and the effective lifetime of the  $B\bar{B}$  background,  $\tau_{B\bar{B}}$ , to the value determined from MC simulation. The fractions  $f_{\text{sig}}$  and  $f_{B\bar{B}}$  are taken from the previous fit. The only floated parameters are  $S$  and  $C$ .

The resolution functions,  $R_{\text{sig}}$  and  $R_{B\bar{B}}$ , are described by convolving three components: detector resolution for  $B_{\text{sig}}$  and  $B_{\text{tag}}$  decay vertices; bias due to the secondary decay vertex of intermediate charm states in  $B_{\text{tag}}$  decays; and a correction to the boost factors due to the small momenta of the  $B$  mesons in the c.m. frame. This last component depends on  $\cos\theta_B^*$ , where  $\theta_B^*$  is the angle in the c.m. frame between the  $B^0$  momentum and the  $\Upsilon(4S)$  boost direction [46]. We model the detector resolution for  $B_{\text{sig}}$  ( $B_{\text{tag}}$ ) vertex on an event-by-event basis, including the dependence on  $\sigma_{\ell_{\text{sig}}}$  ( $\sigma_{\ell_{\text{tag}}}$ ) and the  $\chi^2$  from the vertex fit. The resolution function parameters are determined from MC samples that have been generated with track helix parameters calibrated from data. The data used consist of cosmic ray events in which a cosmic ray track traversing the PXD or SVD is reconstructed as two outgoing tracks from the IP.

For  $B\bar{B}$  background, the  $B_{\text{sig}}$  vertex resolution is the same as that of the signal component due to the high purity of  $K_s^0$  candidates, while the  $B_{\text{tag}}$  vertex suffers from contamination by tracks coming from the background  $B_{\text{sig}}$  decay. We adjust  $\tau_{B\bar{B}}$  in  $\mathcal{P}_{B\bar{B}}$  and parameters of the  $B\bar{B}$  resolution function to account for the smeared vertex position and the typically shorter decay time difference. We model  $\mathcal{P}_{q\bar{q}}(\Delta t)$  using three Gaussian functions, whose shape parameters are determined from a fit to an  $M_{\text{bc}}-\Delta E$  sideband in data defined as  $5.23 \text{ GeV}/c^2 < M_{\text{bc}} < 5.255 \text{ GeV}/c^2$ ,  $-0.5 \text{ GeV} < \Delta E < 0.3 \text{ GeV}$ , and  $(M_{\text{bc}} - 5.23 \text{ GeV}/c^2) < (\Delta E + 0.45 \text{ GeV})/14c^2$ .

The PDF  $P_{\text{TD}}$  depends on  $\cos\theta_B^*$ ,  $\sigma_{\ell_{\text{sig}}}$ ,  $\sigma_{\ell_{\text{tag}}}$ , the vertex-fit  $\chi^2$ 's, and  $r$  (through  $\Delta w$ ), as described in the Supplemental Material [40]. If signal and background events are distributed differently in these variables, then including them in the PDF can introduce bias [47]. Among these variables, only  $r$  and  $\cos\theta_B^*$  differ noticeably between signal and backgrounds, and to alleviate bias we include additional PDFs for them in the likelihood function [47]. The  $r$  and  $\cos\theta_B^*$  distributions for signal and  $B\bar{B}$  background are determined from MC simulation, while those for  $q\bar{q}$  background are taken from the  $M_{\text{bc}}-\Delta E$  sideband in data defined earlier.

For the TI category, the PDF is expressed as

$$\begin{aligned}
 P_{\text{TI}}(q) = & f_{\text{sig}} \left( \frac{1}{2} \right) \left[ 1 - q\Delta w - q(1-2w) \frac{C}{1 + \Delta m_d^2 \tau_{B^0}^2} \right] \\
 & + (1 - f_{\text{sig}}) f_{B\bar{B}} \left( \frac{1 - q\Delta w}{2} \right) \\
 & + (1 - f_{\text{sig}})(1 - f_{B\bar{B}}) \left( \frac{1}{2} \right), \quad (6)
 \end{aligned}$$

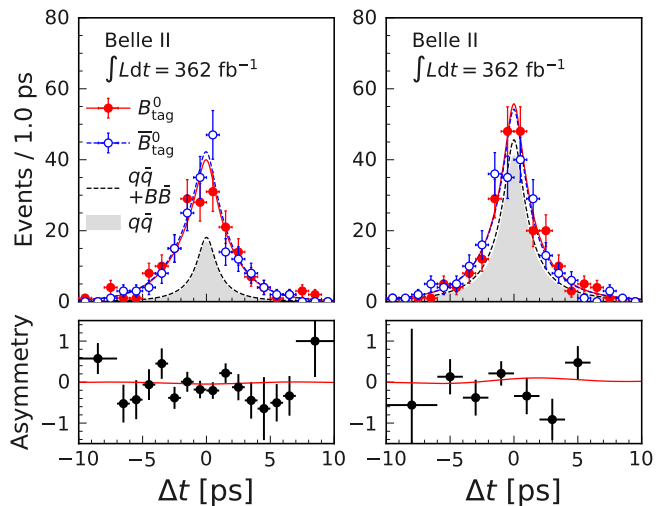


FIG. 2:  $\Delta t$  distributions for MR1 (left) and MR2 (right) with the fit result superimposed. The asymmetry  $[N_{\text{sig}}(B_{\text{tag}}^0) - N_{\text{sig}}(\bar{B}_{\text{tag}}^0)]/[N_{\text{sig}}(B_{\text{tag}}^0) + N_{\text{sig}}(\bar{B}_{\text{tag}}^0)]$  is calculated in each  $\Delta t$  bin using  $sPlot$  [48] and plotted in the bottom panels along with the fit result.

where only the  $C$  parameter is extracted in the fit.

We simultaneously fit the TD and TI samples in the signal-enhanced region, floating the common  $C$  parameter. The results are  $S = 0.00^{+0.27}_{-0.26}$  and  $C = 0.10 \pm 0.13$  for MR1 events, and  $S = 0.04^{+0.45}_{-0.44}$  and  $C = -0.06 \pm 0.25$  for MR2 events. The statistical correlation between  $S$  and  $C$  is  $-0.005$  in MR1 and  $+0.011$  in MR2. Figure 2 shows the  $\Delta t$  distribution along with the fit result. No significant time-dependent asymmetries are observed.

We perform various cross-checks to confirm the validity of our fit procedure. We fit for the  $B^0$  lifetime in the MR1 and MR2 samples and obtain  $1.55 \pm 0.14$  ps and  $1.58 \pm 0.24$  ps, respectively, which are consistent with the world average. We also perform studies of the control mode  $B^+ \rightarrow K_s^0 \pi^+ \gamma$ . The lifetime fit obtains  $1.68 \pm 0.09$  ps, which is consistent with the  $B^+$  lifetime. The difference between  $B^+$  vertices with and without the  $\pi^+$  track is consistent with the  $B_{\text{sig}}$  vertex resolution function. We fit for  $CP$  violation and obtain  $S = 0.05 \pm 0.09$  and  $C = 0.03 \pm 0.05$ , which are consistent with  $S = 0$  and the world average  $C = 0.014 \pm 0.018$  [39].

We consider various sources of systematic uncertainty as listed in Table II. We repeat the analysis with shifted scaling factors for the track momentum and cluster energy and take the deviation from the nominal results as the uncertainty. We consider in a similar manner four sources of systematic uncertainties for the vertex measurements: possible detector misalignments, imperfect understanding of the IP profile measurement [43], corrections to uncertainties on track helix parameters, and the vertex quality selection. We assess the effect of uncertainties in  $w$  and  $\Delta w$  by varying them by their uncer-

tainties and refitting the data. We also simulate the effect of a difference in  $\varepsilon_{\text{tag}}^i$  between  $B_{\text{tag}}^0$  and  $\bar{B}_{\text{tag}}^0$  decays. The systematic uncertainties due to fixed parameters for  $M_{\text{bc}}$ ,  $\Delta E$ , and  $\cos\theta_B^*$  PDFs and  $r$ -bin fractions in signal modeling, including  $f_{\text{sig}}$  and  $f_{B\bar{B}}$ , are also evaluated by refitting. We simulate potential mismodeling of  $M_{\text{bc}} - \Delta E$  distributions and potential bias from the modeling of  $\sigma_{\ell_{\text{sig}}}$ ,  $\sigma_{\ell_{\text{tag}}}$  and the vertex-fit  $\chi^2$ 's [47]. The uncertainties due to limited statistics of the dataset used for KDE are evaluated with the bootstrap method [49].

We consider systematic uncertainties from the modeling and parameters of the  $\Delta t$  resolution function by varying these parameters by their uncertainties and refitting. The differences between these results and our nominal result are taken as systematic uncertainties. We evaluate the uncertainties arising from  $\tau_{B^0}$  and  $\Delta m_d$  in a similar manner, taking their own uncertainties from the PDG [39].

We study the impact of an asymmetry in  $B\bar{B}$  backgrounds using MC simulation. We generate MC samples with asymmetric backgrounds and refit using our nominal (symmetric)  $B\bar{B}$  background PDF. The change in the fit results is assigned as a systematic uncertainty. The asymmetries simulated correspond to the world average values of  $S$ ,  $C$  for  $b \rightarrow sq\bar{q}$  decays, and to maximum values of  $S$ ,  $C$  ( $\pm 1$ ) for  $b \rightarrow s\gamma$  decays.

We evaluate the bias from tag-side interference [50] assuming  $S = C = 0$ . The dominant uncertainties come from the scaling factors for cluster energy, the vertex quality selection criteria, the  $B\bar{B}$  background asymmetry, and the tag-side interference. The total systematic uncertainties, listed in Table II, are calculated as the sum in quadrature of all individual systematic uncertainties.

TABLE II: Summary of systematic uncertainties.

Source	$K^{*0}\gamma$		$K_s^0\pi^0\gamma$	
	$S$	$C$	$S$	$C$
$E$ and $p$ scales	$\pm 0.017$	$\pm 0.015$	$\pm 0.083$	$\pm 0.047$
Vertex measurement	$\pm 0.021$	$\pm 0.009$	$\pm 0.023$	$\pm 0.036$
Flavor tagging	$\pm 0.005$	$^{+0.012}_{-0.009}$	$^{+0.008}_{-0.009}$	$^{+0.013}_{-0.009}$
Signal modeling	$\pm 0.003$	$\pm 0.003$	$\pm 0.032$	$\pm 0.013$
$\Delta t$ resolution function	$\pm 0.014$	$\pm 0.009$	$\pm 0.031$	$\pm 0.013$
$\tau_{B^0}$ and $\Delta m_d$	$< 0.001$	$< 0.001$	$\pm 0.003$	$< 0.001$
$B\bar{B}$ background asym.	$^{+0.007}_{-0.008}$	$\pm 0.011$	$^{+0.030}_{-0.026}$	$^{+0.049}_{-0.051}$
Tag-side interference	$\pm 0.003$	$\pm 0.028$	$\pm 0.003$	$\pm 0.028$
Total	$\pm 0.032$	$^{+0.037}_{-0.038}$	$^{+0.102}_{-0.101}$	$\pm 0.085$

In summary, we have measured the time-dependent  $CP$  asymmetry in  $B^0 \rightarrow K_s^0\pi^0\gamma$  decays using  $(388 \pm 6) \times 10^6$   $B\bar{B}$  events collected by the Belle II detector. These decays are sensitive to right-handed currents arising from BSM physics. We perform these measurements for two  $m(K_s^0\pi^0)$  mass regions corresponding to  $K^{*0} \rightarrow K_s^0\pi^0$  decays and nonresonant decays. We obtain  $CP$ -violating

parameters

$$S = 0.00_{-0.26}^{+0.27} \pm 0.03, \quad C = 0.10 \pm 0.13 \pm 0.04 \quad (7)$$

for the  $K^{*0}$  resonant region and

$$S = 0.04_{-0.44}^{+0.45} \pm 0.10, \quad C = -0.06 \pm 0.25 \pm 0.09 \quad (8)$$

for the nonresonant region, where the uncertainties are statistical and systematic, respectively. These results have improved precision with respect to previous measurements [17, 18] and are consistent with SM predictions. The improvements mostly result from a refined  $K_s^0$  identification algorithm and a large-acceptance silicon vertex detector [22].

This work, based on data collected using the Belle II detector, which was built and commissioned prior to March 2019, was supported by Higher Education and Science Committee of the Republic of Armenia Grant No. 23LCG-1C011; Australian Research Council and Research Grants No. DP200101792, No. DP210101900, No. DP210102831, No. DE220100462, No. LE210100098, and No. LE230100085; Austrian Federal Ministry of Education, Science and Research, Austrian Science Fund No. P 31361-N36 and No. J4625-N, and Horizon 2020 ERC Starting Grant No. 947006 ‘‘InterLeptons’’; Natural Sciences and Engineering Research Council of Canada, Compute Canada and CANARIE; National Key R&D Program of China under Contract No. 2022YFA1601903, National Natural Science Foundation of China and Research Grants No. 11575017, No. 11761141009, No. 11705209, No. 11975076, No. 12135005, No. 12150004, No. 12161141008, and No. 12175041, and Shandong Provincial Natural Science Foundation Project ZR2022JQ02; the Czech Science Foundation Grant No. 22-18469S; European Research Council, Seventh Framework PIF-GA-2013-622527, Horizon 2020 ERC-Advanced Grants No. 267104 and No. 884719, Horizon 2020 ERC-Consolidator Grant No. 819127, Horizon 2020 Marie Skłodowska-Curie Grant Agreement No. 700525 ‘‘NIOBE’’ and No. 101026516, and Horizon 2020 Marie Skłodowska-Curie RISE project JENNIFER2 Grant Agreement No. 822070 (European grants); L’Institut National de Physique Nucléaire et de Physique des Particules (IN2P3) du CNRS and L’Agence Nationale de la Recherche (ANR) under grant ANR-21-CE31-0009 (France); BMBF, DFG, HGF, MPG, and AvH Foundation (Germany); Department of Atomic Energy under Project Identification No. RTI 4002, Department of Science and Technology, and UPES SEED funding programs No. UPES/R&D-SEED-INFRA/17052023/01 and No. UPES/R&D-SOE/20062022/06 (India); Israel Science Foundation Grant No. 2476/17, U.S.-Israel Binational Science Foundation Grant No. 2016113, and Israel Ministry of Science Grant No. 3-16543; Istituto Nazionale di Fisica Nucleare and the Research

Grants BELLE2; Japan Society for the Promotion of Science, Grant-in-Aid for Scientific Research Grants No. 16H03968, No. 16H03993, No. 16H06492, No. 16K05323, No. 17H01133, No. 17H05405, No. 18K03621, No. 18H03710, No. 18H05226, No. 19H00682, No. 20H05850, No. 20H05858, No. 22H00144, No. 22K14056, No. 22K21347, No. 23H05433, No. 26220706, and No. 26400255, the National Institute of Informatics, and Science Information NETWORK 5 (SINET5), and the Ministry of Education, Culture, Sports, Science, and Technology (MEXT) of Japan; National Research Foundation (NRF) of Korea Grants No. 2016R1D1A1B02012900, No. 2018R1A2B3003643, No. 2018R1A6A1A06024970, No. 2019R1I1A3A01058933, No. 2021R1A6A1A-03043957, No. 2021R1F1A1060423, No. 2021R1F1A-1064008, No. 2022R1A2C1003993, and No. RS-2022-00197659, Radiation Science Research Institute, Foreign Large-Size Research Facility Application Supporting project, the Global Science Experimental Data Hub Center of the Korea Institute of Science and Technology Information and KREONET/GLORIAD; Universiti Malaya RU grant, Akademi Sains Malaysia, and Ministry of Education Malaysia; Frontiers of Science Program Contracts No. FOINS-296, No. CB-221329, No. CB-236394, No. CB-254409, and No. CB-180023, and SEP-CINVESTAV Research Grant No. 237 (Mexico); the Polish Ministry of Science and Higher Education and the National Science Center; the Ministry of Science and Higher Education of the Russian Federation and the HSE University Basic Research Program, Moscow; University of Tabuk Research Grants No. S-0256-1438 and No. S-0280-1439 (Saudi Arabia); Slovenian Research Agency and Research Grants No. J1-9124 and No. P1-0135; Agencia Estatal de Investigacion, Spain Grant No. RYC2020-029875-I and Generalitat Valenciana, Spain Grant No. CIDEGENT/2018/020; National Science and Technology Council, and Ministry of Education (Taiwan); Thailand Center of Excellence in Physics; TUBITAK ULAKBIM (Turkey); National Research Foundation of Ukraine, Project No. 2020.02/0257, and Ministry of Education and Science of Ukraine; the U.S. National Science Foundation and Research Grants No. PHY-1913789 and No. PHY-2111604, and the U.S. Department of Energy and Research Awards No. DE-AC06-76RLO1830, No. DE-SC0007983, No. DE-SC0009824, No. DE-SC0009973, No. DE-SC0010007, No. DE-SC0010073, No. DE-SC0010118, No. DE-SC0010504, No. DE-SC0011784, No. DE-SC0012704, No. DE-SC0019230, No. DE-SC0021274, No. DE-SC0021616, No. DE-SC0022350, No. DE-SC0023470; and the Vietnam Academy of Science and Technology (VAST) under Grants No. NVCC.05.12/22-23 and No. DL0000.02/24-25.

These acknowledgements are not to be interpreted as an endorsement of any statement made by any of our

institutes, funding agencies, governments, or their representatives.

We thank the SuperKEKB team for delivering high-luminosity collisions; the KEK cryogenics group for the efficient operation of the detector solenoid magnet; the KEK computer group and the NII for on-site computing support and SINET6 network support; and the raw-data centers at BNL, DESY, GridKa, IN2P3, INFN, and the University of Victoria for off-site computing support.

- 
- [1] S. Bertolini, F. Borzumati, A. Masiero, and G. Ridolfi, *Nucl. Phys. B* **353**, 591 (1991).
  - [2] P. L. Cho and M. Misiak, *Phys. Rev. D* **49**, 5894 (1994).
  - [3] K. Fujikawa and A. Yamada, *Phys. Rev. D* **49**, 5890 (1994).
  - [4] D. Atwood, M. Gronau, and A. Soni, *Phys. Rev. Lett.* **79**, 185 (1997).
  - [5] D. Atwood, T. Gershon, M. Hazumi, and A. Soni, *Phys. Rev. D* **71**, 076003 (2005).
  - [6] M. Blanke, B. Shakya, P. Tanedo, and Y. Tsai, *J. High Energy Phys.* **08** (2012), 038.
  - [7] D. Becirevic, E. Kou, A. Le Yaouanc, and A. Tayduganov, *J. High Energy Phys.* **08** (2012), 090.
  - [8] Y. Shimizu, M. Tanimoto, and K. Yamamoto, *Phys. Rev. D* **87**, 056004 (2013).
  - [9] E. Kou, C.-D. Lü, and F.-S. Yu, *J. High Energy Phys.* **12** (2013), 102.
  - [10] R. Malm, M. Neubert, and C. Schmell, *J. High Energy Phys.* **04** (2016), 042.
  - [11] H. Eberl, K. Hidaka, E. Ginina, and A. Ishikawa, *Phys. Rev. D* **104**, 075025 (2021).
  - [12] Charge-conjugate modes are included unless explicitly stated otherwise.
  - [13] M. Matsumori and A. I. Sanda, *Phys. Rev. D* **73**, 114022 (2006).
  - [14] P. Ball, G. W. Jones, and R. Zwicky, *Phys. Rev. D* **75**, 054004 (2007).
  - [15] B. Grinstein, Y. Grossman, Z. Ligeti, and D. Pirjol, *Phys. Rev. D* **71**, 011504 (2005).
  - [16] B. Grinstein and D. Pirjol, *Phys. Rev. D* **73**, 014013 (2006).
  - [17] Y. Ushiroda *et al.* (Belle Collaboration), *Phys. Rev. D* **74**, 111104 (2006).
  - [18] B. Aubert *et al.* (BABAR Collaboration), *Phys. Rev. D* **78**, 071102 (2008).
  - [19] I. Adachi *et al.* (Belle II Collaboration), arXiv:2407.00965 [hep-ex] (2024).
  - [20] T. Abe *et al.* (Belle II Collaboration), arXiv:1011.0352 [physics.ins-det] (2010).
  - [21] K. Akai, K. Furukawa, and H. Koiso (SuperKEKB Group), *Nucl. Instrum. Methods Phys. Res., Sect. A* **907**, 188 (2018).
  - [22] K. Adamczyk *et al.* (Belle II SVD Collaboration), *J. Instrum.* **17**, P11042 (2022).
  - [23] D. Kotchetkov *et al.*, *Nucl. Instrum. Methods Phys. Res., Sect. A* **941**, 162342 (2019).
  - [24] F. Abudinén *et al.* (Belle II Collaboration), *Eur. Phys. J. C* **82**, 283 (2022).
  - [25] A. B. Carter and A. I. Sanda, *Phys. Rev. Lett.* **45**, 952

- (1980).
- [26] A. B. Carter and A. I. Sanda, Phys. Rev. D **23**, 1567 (1981).
  - [27] I. I. Y. Bigi and A. I. Sanda, Nucl. Phys. B **193**, 85 (1981).
  - [28] Here, we neglect  $CP$  violation in  $B^0-\bar{B}^0$  mixing.
  - [29] The coefficients ( $S, -C$ ) are written ( $S, A$ ) elsewhere.
  - [30] A. L. Kagan and M. Neubert, Eur. Phys. J. C **7**, 5 (1999).
  - [31] D. J. Lange, Nucl. Instrum. Methods Phys. Res., Sect. A **462**, 152 (2001).
  - [32] S. Jadach, B. F. L. Ward, and Z. Wąs, Comput. Phys. Commun. **130**, 260 (2000).
  - [33] T. Sjöstrand *et al.*, Comput. Phys. Commun. **191**, 159 (2015).
  - [34] S. Jadach, J. H. Kuhn, and Z. Wąs, Comput. Phys. Commun. **64**, 275 (1990).
  - [35] S. Agostinelli *et al.* (GEANT4 Collaboration), Nucl. Instrum. Methods Phys. Res., Sect. A **506**, 250 (2003).
  - [36] T. Kuhr *et al.* (Belle II Framework Software Group), Comput. Softw. Big Sci. **3**, 1 (2019).
  - [37] R. Storn and K. Price, J. Global Optim. **11**, 341 (1997).
  - [38] Refer Belle II publication #41.
  - [39] R. L. Workman *et al.* (Particle Data Group), PTEP **2022**, 083C01 (2022).
  - [40] See Supplemental Material at ...
  - [41] J. F. Krohn *et al.* (Belle II Analysis Software Group), Nucl. Instrum. Methods Phys. Res., Sect. A **976**, 164269 (2020).
  - [42] S. Dey and A. Soffer, Springer Proc. Phys. **248**, 411 (2020).
  - [43] I. Adachi *et al.* (Belle II Collaboration), arXiv:2302.12898 [hep-ex] (2023). The calibration described in this note has been updated with the larger  $362\text{ fb}^{-1}$  dataset used in this analysis.
  - [44] K. S. Cranmer, Comput. Phys. Commun. **136**, 198 (2001).
  - [45] H. Albrecht *et al.* (ARGUS Collaboration), Phys. Lett. B **241**, 278 (1990).
  - [46] H. Tajima *et al.*, Nucl. Instrum. Methods Phys. Res., Sect. A **533**, 370 (2004).
  - [47] G. Punzi, eConf **C030908**, WELT002 (2003).
  - [48] M. Pivk and F. R. Le Diberder, Nucl. Instrum. Methods Phys. Res., Sect. A **555**, 356 (2005).
  - [49] B. Efron, The Annals of Statistics **7**, 1 (1979).
  - [50] O. Long, M. Baak, R. N. Cahn, and D. P. Kirkby, Phys. Rev. D **68**, 034010 (2003). We take  $r' = 0.015$  and  $\delta = \pm\pi/2$  to evaluate this systematic effect.
  - [51] A. Khotanzad and Y. Hong, IEEE Trans. Pattern Anal. Mach. Intell. **12**, 489 (1990).
  - [52] G. C. Fox and S. Wolfram, Phys. Rev. Lett. **41**, 1581 (1978).
  - [53] Ed. A. J. Bevan, B. Golob, Th. Mannel, S. Prell, and B. D. Yabsley, Eur. Phys. J. **C74**, 3026 (2014).
  - [54] S. Brandt *et al.*, Phys. Lett. **12**, 57 (1964).
  - [55] E. Farhi, Phys. Rev. Lett. **39**, 1587 (1977).
  - [56] S. H. Lee *et al.* (Belle Collaboration), Phys. Rev. Lett. **91**, 261801 (2003).
  - [57] D. M. Asner *et al.* (CLEO Collaboration), Phys. Rev. **D53**, 1039 (1996).



## SUPPLEMENTAL MATERIAL

### $\pi^0$ BDT classifier

The BDT classifier used to identify  $B_{\text{sig}}$  candidates is trained using simulated samples consisting of approximately 180 000 true and misreconstructed  $\pi^0$  candidates. These candidates are required to satisfy  $|M_{\gamma\gamma} - 134 \text{ MeV}/c^2| < 27 \text{ MeV}/c^2$  and  $p_{\gamma\gamma} > 420 \text{ MeV}/c$ . The main background is fake  $\pi^0$  candidates reconstructed from spurious photons. We use the following nine variables for training: the energies of both  $\gamma$  candidates; properties of the ECL cluster of the less energetic  $\gamma$ , namely, the azimuthal angle, number of hits,  $E_1/E_9$  and  $E_9/E_{21}$  (the ratios of energy deposited in  $1 \times 1$ ,  $3 \times 3$ , and  $5 \times 5 - 4$  (at the corners) square bundle of crystals), and the MVA output for  $\gamma - K_L^0$  separation using Zernike moments [51]; the helicity angle and the invariant mass of the  $\pi^0$ . Figure 3 shows distributions of the BDT output for signal and background in an independent test sample.

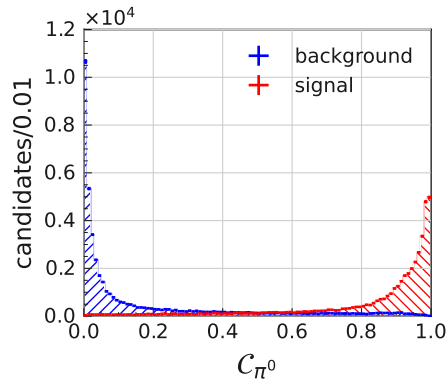


FIG. 3: The BDT output,  $C_{\pi^0}$ , distributions for signal and background.

### $q\bar{q}$ suppression

To separate signal events from  $q\bar{q}$  background events, we train a BDT classifier using approximately 770 000  $B^0$  candidates from signal and  $q\bar{q}$  simulated samples. We apply the following selections on  $B_{\text{tag}}$  daughters: at least 1 CDC hit and  $p^* < 3.2 \text{ GeV}/c$  for tracks, and  $p > 50 \text{ MeV}/c$  and  $p^* < 3.2 \text{ GeV}/c$  for ECL clusters. The following 29 variables are used as input: the ratio between the second and zeroth Fox–Wolfram moments [52]; the cosine of the angle between the thrust axis of  $B_{\text{sig}}$  and  $B_{\text{tag}}$  [53]; the thrust scalars [54, 55] of  $B_{\text{sig}}$  and  $B_{\text{tag}}$ ; the sum of the magnitudes of the transverse momenta of all the particles in the event; the missing mass squared of the event, defined as  $M_{\text{miss}}^2 = (E_{e^+e^-} - \sum_i E_i)^2 - \sum_i |\mathbf{p}_i|^2$ , where  $E_{e^+e^-}$  is the sum of the  $e^+e^-$  beam energies,  $E_i$

and  $\mathbf{p}_i$  are the energy and momentum of particle  $i$ , and the summation of  $i$  runs over all particles; 14 Super Fox–Wolfram moments [56]; and 9 CLEO cones [57]. As the flavor tagging is optimized for  $B\bar{B}$  events, a high value of  $r$  indicates lower contamination from  $q\bar{q}$  background. To maximize the selection performance, we set different thresholds on the BDT output for each  $r$ -bin. Figure 4 shows distributions of classifiers for MR1 and MR2 for signal and background for independent test samples.

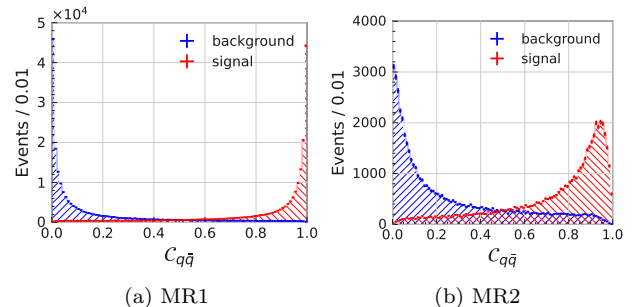


FIG. 4: Distributions of  $q\bar{q}$  suppression BDT outputs for (a) MR1 and (b) MR2 regions, for signal and background.

### $\Delta t$ resolution functions

The resolution functions  $R_{\text{sig}}$  and  $R_{B\bar{B}}$  are the convolutions of four functions [46],

$$R_{\text{vtx sig}} \otimes R_{\text{vtx tag}} \otimes R_{D \text{ tag}} \otimes R_{\text{boost}}, \quad (9)$$

where  $R_{\text{vtx sig}}$  and  $R_{\text{vtx tag}}$  are detector resolutions for  $B_{\text{sig}}$  and  $B_{\text{tag}}$  decay vertices,  $R_{D \text{ tag}}$  represents the bias due to the secondary decay vertices of intermediate charm states in  $B_{\text{tag}}$  decay, and  $R_{\text{boost}}$  is the correction to the boost factors due to the small but nonzero momenta of the  $B$  mesons in the c.m. frame.

The detector resolutions  $R_{\text{vtx sig}}$  and  $R_{\text{vtx tag}}$  are modeled with the sum of two Gaussian functions:

$$R_{\text{vtx sig (tag)}}(\delta\ell) = (1 - f_{\text{tail}})G(\delta\ell; 0, s_{\text{main}}\sigma_\ell) + f_{\text{tail}}G(\delta\ell; 0, s_{\text{tail}}\sigma_\ell), \quad (10)$$

where  $\delta\ell$  and  $\sigma_\ell$  in  $R_{\text{vtx sig}}$  ( $R_{\text{vtx tag}}$ ) are the residual and the uncertainty of  $\ell_{\text{sig}}$  ( $\ell_{\text{tag}}$ ),  $G(x; \mu, \sigma)$  is a Gaussian function with mean  $\mu$  and standard deviation  $\sigma$ ,  $f_{\text{tail}}$  is the fraction of the tail component, and  $s_{\text{main}}$  and  $s_{\text{tail}}$  are scaling factors for the uncertainty. The parameters  $f_{\text{tail}}$  and  $s_{\text{main}}$  in  $R_{\text{vtx sig}}$  ( $s_{\text{main}}$  and  $s_{\text{tail}}$  in  $R_{\text{vtx tag}}$ ) are modeled with a linear dependence on  $(\chi_{\text{tracks}}^2)^{\text{sig}}$  or  $(\chi^2/\nu_{\text{d.f.}})^{\text{tag}}$ , which are the  $B_{\text{sig}}$  vertex fit  $\chi^2$  calculated for the  $K_S^0 \rightarrow \pi^+\pi^-$  tracks and the reduced  $\chi^2$  for  $B_{\text{tag}}$  vertex fit. These dependencies correct for underestimated vertex position uncertainty in case a track is reconstructed using incorrect hits.

The bias due to the secondary decay vertex  $R_{D\text{tag}}$  is modeled by the sum of two exponential functions and a delta function:

$$R_{D\text{tag}}(\delta\ell_{\text{tag}}) = f_\delta\delta(\delta\ell_{\text{tag}}) + (1 - f_\delta)f_p E_p(\delta\ell_{\text{tag}}; \tau_{\text{np}}\sigma_{\ell_{\text{tag}}}) + (1 - f_\delta)(1 - f_p)E_n(\delta\ell_{\text{tag}}; \tau_{\text{np}}\sigma_{\ell_{\text{tag}}}), \quad (11)$$

where  $E_p$  and  $E_n$  are one-sided exponential functions,

$$E_p(x; \tau) = \frac{1}{\tau} \exp\left(-\frac{x}{\tau}\right) \text{ for } x > 0, \text{ otherwise } 0, \quad (12)$$

$$E_n(x; \tau) = \frac{1}{\tau} \exp\left(+\frac{x}{\tau}\right) \text{ for } x \leq 0, \text{ otherwise } 0, \quad (13)$$

and  $f_\delta$ ,  $f_p$ , and  $\tau_{\text{np}}$  are functions of  $(\chi^2/\nu_{\text{d.f.}})^{\text{tag}}$  or  $\sigma_{\ell_{\text{tag}}}$ .

The boost factor correction  $R_{\text{boost}}$  is described in Ref. [46]:

$$R_{\text{boost}}(\Delta t - \Delta t_{\text{true}}) = \begin{cases} E_p(\Delta t - (a\Delta t_{\text{true}} + c_k|\Delta t_{\text{true}}|); |c_k|\tau_{B^0}) & (\cos\theta_B^* > 0) \\ \delta(\Delta t - a\Delta t_{\text{true}}) & (\cos\theta_B^* = 0), \\ E_n(\Delta t - (a\Delta t_{\text{true}} + c_k|\Delta t_{\text{true}}|); |c_k|\tau_{B^0}) & (\cos\theta_B^* < 0) \end{cases}, \quad (14)$$

where  $\Delta t_{\text{true}}$  is the true difference between the proper decay times of  $B_{\text{sig}}$  and  $B_{\text{tag}}$ ,  $\Delta t$  is calculated with true

$\ell_{\text{sig}}$  and  $\ell_{\text{tag}}$ , and

$$a = \frac{E_B^*}{m_{B^0}}, \quad c_k = \frac{|\mathbf{p}_B^*| \cos\theta_B^*}{\beta m_{B^0}}, \quad (15)$$

with  $m_{B^0}$  being the nominal  $B^0$  mass [39].

In total, we have 17 parameters: two in  $f_{\text{tail}}$ , two in  $s_{\text{main}}$ , and  $s_{\text{tail}}$  for  $R_{\text{vtxsig}}$ ;  $f_{\text{tail}}$ , two in  $s_{\text{main}}$ , and two in  $s_{\text{tail}}$  for  $R_{\text{vtxtag}}$ ; and two in  $f_\delta$ , two in  $f_p$ , and three in  $\tau_{\text{np}}$  for  $R_{D\text{tag}}$ . These are all fixed to values obtained from fitting MC samples.

We model the  $\Delta t$  PDF for  $q\bar{q}$  background with the sum of three Gaussian functions:

$$P_{q\bar{q}}(\Delta t; X^2, \sigma_{\Delta t}) = \left(\frac{1}{2}\right) \left[ (1 - f_2)(1 - f_3)G(\Delta t; 0, (s_1^0 + s_1^1 X^2)\sigma_{\Delta t}) + f_2(1 - f_3)G(\Delta t; 0, (s_2^0 + s_2^1 X^2)\sigma_{\Delta t}) + f_3G(\Delta t; 0, s_3\sigma_{\Delta t}), \right] \quad (16)$$

where  $X^2$  is the average reduced  $\chi^2$  and  $\sigma_{\Delta t}$  is the  $\Delta t$  uncertainty:

$$X^2 = \frac{(\chi_{\text{tracks}}^2)^{\text{sig}}/1.6 + (\chi^2/\nu_{\text{d.f.}})^{\text{tag}}}{2}, \quad (17)$$

$$\sigma_{\Delta t} = \frac{\sqrt{(\sigma_{\ell_{\text{sig}}})^2 + (\sigma_{\ell_{\text{tag}}})^2}}{\beta\gamma}. \quad (18)$$

The factor of 1.6 in Eq. (17) accounts for the effective number of degrees of freedom for the  $K_s^0$  vertex in the  $B^0$  vertex fit. The seven free parameters, namely  $f_2$ ,  $f_3$ ,  $s_1^0$ ,  $s_1^1$ ,  $s_2^0$ ,  $s_2^1$ , and  $s_3$ , are determined from a fit to events in the  $M_{\text{bc}} - \Delta E$  sideband.